Systems/Circuits

μ-Opioid Receptor Activation Reduces Glutamate Release in the PreBötzinger Complex in Organotypic Slice Cultures

Anders B. Jørgensen, Camilla Mai Rasmussen, and Jens C. Rekling
Department of Neuroscience, University of Copenhagen, Copenhagen N DK-2200, Denmark

The inspiratory rhythm generator, located in the brainstem preBötzinger complex (preBötC), is dependent on glutamatergic signaling and is affected profoundly by opioids. Here, we used organotypic slice cultures of the newborn mouse brainstem of either sex in combination with genetically encoded sensors for Ca^{2+}, glutamate, and GABA to visualize Ca^{2+}, glutamatergic and GABAergic signaling during spontaneous rhythm and in the presence of DAMGO. During spontaneous rhythm, the glutamate sensor SF-iGluSnFR.A184S revealed punctate synapse-like fluorescent signals along dendrites and somas in the preBötC with decay times that were prolonged by the glutamate uptake blocker (TFB-TBOA). The GABA sensor iGABASnFR showed a more diffuse fluorescent signal during spontaneous rhythm. Rhythmic Ca^{2+}- and glutamate transients had an inverse relationship between the spontaneous burst frequency and the burst amplitude of the Ca^{2+} and glutamate signals. A similar inverse relationship was observed when bath applied DAMGO reduced spontaneous burst frequency and increased the burst amplitude of Ca^{2+}, glutamate, and GABA transient signals. However, a hypoxic challenge reduced both burst frequency and Ca^{2+} transient amplitude. Using a cocktail that blocked glutamatergic, GABAergic, and glycinergic transmission to indirectly measure the release of glutamate/GABA in response to an electrical stimulus, we found that DAMGO reduces the release of glutamate in the preBötC but has no effect on GABA release. This suggest that the opioid mediated slowing of respiratory rhythm involves presynaptic reduction of glutamate release, which would impact the ability of the network to engage in recurrent excitation, and may result in the opioid-induced slowing of inspiratory rhythm.

Key words: **breathing; GABA; genetically-encoded sensors; iGluSnFR; opioids; respiration**

Significance Statement

Opioids slow down breathing rhythm by affecting neurons in the preBötzinger complex (preBötC) and other brainstem regions. Here, we used cultured slices of the preBötC to better understand this effect by optically recording Ca^{2+}, glutamate, and GABA transients during preBötC activity. Spontaneous rhythm showed an inverse relationship between burst frequency and burst amplitude in the Ca^{2+} and glutamate signals. Application of the opioid DAMGO slowed the rhythm, with a concomitant increase in Ca^{2+}, glutamate, and GABA signals. When rhythm was blocked pharmacologically, DAMGO reduced the presynaptic release of glutamate, but not GABA. These data suggest the mechanism of action of opioids involves presynaptic reduction of glutamate release, which may play an important role in the opioid-induced slowing of inspiratory rhythm.

Introduction

Inspiratory rhythm is dependent on glutamatergic neurons in the preBötzinger complex (preBötC) that form local excitatory networks (Richter and Smith, 2014; Ikeda et al., 2017; Del Negro et al., 2018; Ramirez and Baertsch, 2018). The circuit connecting these glutamatergic neurons is unknown, but likely include recurrent connections and reciprocal connections to GABAergic and glycinergic neurons in the preBötC (Rekling et al., 2000; Pace et al., 2007; Bouvier et al., 2010; Koizumi et al., 2013, 2016; Guerrier et al., 2015; Kottick and Del Negro, 2015; Song et al., 2015; Baertsch et al., 2018; Baertsch and Ramirez, 2019). Studying the involvement of glutamatergic transmission in respiratory rhythm generation has relied on electrophysiological and pharmacological methods. However, advances in genetically-encoded Ca^{2+} and transmitter sensors (Dong et al., 2022) permit optical studies of neuronal activity and transmitter dynamics in circuits such as the preBötC. Here, we combine the use of organotypic slice cultures and AAV-mediated expression of the glutamate sensor SF-iGluSnFR.A184S (Marvin et al., 2018) to directly visualize glutamate transients in the preBötC. In addition, we use the Ca^{2+} sensors jGCaMP7f/jRCaMP1b and the GABA sensor iGABASnFR to gain a better understanding of the synaptic

Received July 13, 2022; revised Aug. 22, 2022; accepted Sep. 7, 2022.
Author contributions: A.B.J., C.M.R., and J.C.R. designed research; A.B.J., C.M.R., and J.C.R. performed research; A.B.J., C.M.R., and J.C.R. analyzed data; C.M.R. edited the paper; A.B.J. and J.C.R. wrote the paper.
This work was supported by The Danish Research Council and The Lundbeck Foundation.
The authors declare no competing financial interests.
Correspondence should be addressed to Jens C. Rekling at jrekling@sund.ku.dk.
https://doi.org/10.1523/JNEUROSCI.1369-22.2022

dynamics during opioid-mediated slowing of the preBötC rhythm.

Opioid-mediated signaling plays an important role in the control of breathing (Palkovic et al., 2020; Ramirez et al., 2021; Bodnar, 2022). Four regions appear to be involved in opioid-related modulation of breathing, the parabrachial nucleus/Kölliker–Fuse complex, the preBötC, the nucleus tractus solitarius (NTS), and the caudal medullary raphe (Levitt et al., 2015; Miller et al., 2017; Bachmutsky et al., 2020; Varga et al., 2020; Liu et al., 2021; Palkovic et al., 2022). The preBötC network becomes active during the last third of gestation in mice, and opioids have a depressant action on the isolated preBötC already manifested at this embryonic stage (Chevalier et al., 2016). In juvenile and adult animals, opioids injected into the preBötC produce variable effects raging from respiratory depression to increased breathing frequency (Ramirez et al., 2021). However, a consistent depressant action of opioids is seen on preBötC-driven rhythm in reduced in vitro preparations, and the discrepancy has been attributed to neuromodulatory mechanisms within the preBötC, capable of compensating for the depressant effects of opioids in intact brains.

The cellular mechanisms that underlie the depressant actions of opioids on respiratory rhythm are not fully understood, but are hypothesized to involve postsynaptic hyperpolarization and presynaptic control of transmitter release. In the preBötC opioids act through μ-opioid receptors (MORs) which are only sparsely expressed (Hayes et al., 2017; Bachmutsky et al., 2020; Kallurkar et al., 2022), and application of MOR agonists lead to postsynaptic hyperpolarization (Gray et al., 1999; Haji et al., 2003; Inyushkin, 2007; Montandon et al., 2011, 2016; Baertsch et al., 2021; Ramirez et al., 2021). However, postsynaptic hyperpolarization is not sufficient alone to explain the reduction in breathing frequency, since optogenetically-induced silencing of interburst spike activity of MOR-expressing preBötC neurons does not produce an opioid-like effect on respiratory frequency (Baertsch et al., 2021). Commissural preBötC neurons show reduced EPSP amplitude after DAMGO exposure (Baertsch et al., 2021), and the slope of preBötC EPSPs evoked from contralateral preBötC electrical stimulation is reduced by DAMGO (Takeda et al., 2001). Miniature EPSPs show a reduced spontaneous frequency when DAMGO is present (Wei and Ramirez, 2019). Together, these data suggests that opioids might affect glutamatergic transmission presynaptically in preBötC neurons. Here, we confirm this using organotypic slice cultures from newborn mice in combination with genetically encoded sensors for Ca^{2+}, glutamate, and GABA, demonstrating a depressant action of DAMGO on the presynaptic release of glutamate, but not GABA, in the preBötC.

Materials and Methods

Preparation of organotypic brainstem slice cultures

All animal procedures were performed in accordance with the University of Copenhagen animal care committee's regulations. Organotypic slice cultures, containing the preBötC, were prepared using United States Naval Medical Research Institute (NMRI) mice postnatal ages postnatal day (P)2.5–P10.5. Following complete anesthesia with isoflurane (Baxter), mice of both sex were euthanized and immediately hereafter dissected in sterile-filtered chilled dissection artificial CSF (aCSF) containing the following: 135 mM glycerol, 2.5 mM KCl, 1.2 mM NaH_2PO_4, 30 mM $NaHCO_3$, 5 mM HEPES acid, 15 mM HEPES base, 25 mM D-glucose, 5 mM sodium ascorbate, 2 mM thiourea, 3 mM sodium pyruvate, 10 mM $MgSO_4$, and 0.5 mM $CaCl_2$; final osmolarity adjusted to 300–310 mOsm using glycerol or water, pH 7.3, equilibrated by bubbling with 95% O_2/5% CO_2. Using a vibrating microtome (ThermoFisher Scientific Microm 650V, RRID:SCR_008452) a single, transverse medullary brainstem slice was cut (400-μm thickness) at the level of the preBötC. After the acute preparation, one to four slice cultures were placed on semi-porous culture well inserts using the Stoppini interface method (Millipore catalog #PIC03050, RRID:SCR_008983). Cultures were kept in organotypic culture media containing: 95% Neurobasal-A medium (ThermoFisher Scientific, catalog #10888-022, RRID:SCR_008452), 2% B-27 supplement (ThermoFisher Scientific, catalog #17504044, RRID:SCR_008452), 2 mM GlutaMAX (ThermoFisher Scientific, catalog #35050-038, RRID:SCR_008452), 0.5 μM T3 (Sigma-Aldrich, catalog #T6397, RRID:SCR_008988), 0.5 μM T4 (Sigma-Aldrich, catalog #T1775, RRID:SCR_008988), 10 μg/l GDNF (PeproTech, catalog #450-44, RRID:SCR_006802), 200 U/ml penicillin, 5 μg/ml streptomycin, and 10 mM HEPES and pH was set at 7.25. The cultures were kept in a humidified incubator at 35°C, with 5% CO_2 until their use for experimentation and given fresh medium every 48 h. For the first 3 d, the cultures were treated with 10 μM MK-801 (Sigma-Aldrich, catalog #M107, RRID:SCR_008988).

Neuronal labeling with SF-iGluSnFR.A184S, iGABASnFR, and GECIs

Organotypic slice cultures were transduced with viral AAV constructs containing the genes for SF-iGluSnFR.A184S (pAAV.hSynapsin.SF-SF-iGluSnFR.A184S.A184S, AAV-retrograde, Addgene, catalog #06174-AAVrg, RRID:Addgene_106174, abbr: AAVRetro-SF-iGluSnFR.A184S), iGABASnFR (pAAV.hSynap.iGABASnFR, AAV1, Addgene, catalog #112159-AAV1, RRID:Addgene_112159, abbr: AAV1-iGABASnFR), jGCaMP7f (pGP-AAV-syn-jGCaMP7f-WPRE, AAV retrograde, Addgene, catalog#:104488, RRID:Addgene_104488, abbr: AAVRetro-jGCaMP7f) and jRCaMP1b (pAAV.Syn.NES-jRCaMP1b.WPRE.SV40, AAV9, Addgene, catalog #100851, RRID:Addgene_100851, Abbr: AAV9-jRCaMP1b). The AAV viruses were diluted in ultrapure water and cultures were transduced the day after they were prepared, either by adding a drop of virus solution directly on top of a slice culture, infecting the entire culture, or by injection of ~50-nl virus solution in the ventrolateral area using a single-barrel glass micropipette, primarily infecting the preBötC area. AAVRetro-SF-iGluSnFR.A184S or AAV1-iGABASnFR (~2×10^{12} vg/ml) were bilateral-injected, and for co-transductions with GECIs, slices were first unilateral-injected with AAVRetro-jGCaMP7f (~2×10^{12} vg/ml) in the right ventrolateral area followed by a drop transduction with AAV9-jRCaMP1b (~3×10^{12} vg/ml) of the entire culture the following day. We suspect that drop transduction of the entire culture and local injections may lead to different expression levels. Cultures were used for experiments 9–35 d (average: 17.5) after transduction.

Recirculating aCSF and electrophysiology

Spontaneous rhythmic activity generated in the slice cultures was recorded in an in vitro chamber with a recirculating system (29°C) filled with a high-excitability aCSF (high-aCSF) containing the following: 124 mM NaCl, 3 mM KCl, 5 mM KH_2PO_4, 25 mM $NaHCO_3$, 25 mM D-glucose, 1 mM ascorbic acid, 1 mM $MgCl_2$, and 1.5 mM $CaCl_2$ (all from Sigma-Aldrich, RRID:SCR_008988), with pH 7.4, equilibrated by bubbling with 95% O_2/5% CO_2. In the TFB-TBOA experiments a low-aCSF composed of the following: 124 mM NaCl, 2 mM KCl, 1.25 mM NaH_2PO_4, 25 mM $NaHCO_3$, 25 mM D-glucose, 1 mM ascorbic acid, 6 mM $MgCl_2$, and 3 mM $CaCl_2$ (all from Sigma-Aldrich, RRID:SCR_008988), with pH 7.4, equilibrated by bubbling with 95% O_2/5% CO_2, was used to stop spontaneous rhythmic activity in the slice.

Electrical field stimulation was done using a sharp bipolar tungsten electrode, +/− poles ~500 μm apart. After the preBötC had been identified and spontaneous rhythm was brought to cessation by adding NBQX, CPP, gabazine, and strychnine, the bipolar electrode was placed on the culture surface encompassing the core preBötC. Trains of unipolar pulses with constant voltage (interval: 20 ms, pulse duration: 2 ms, amplitude: 4.5–6 V) were used to stimulate fibers and somas between the two poles, using a stimulus isolation unit gated by a waveform generator (A.M.P.I. ISO-Flex isolator, RRID:SCR_018945, AMPI Master 8 generator, RRID:SCR_018889).

Electrical microstimulations were done with micropipettes that were pulled from filamented theta capillary glass (OD/ID 1.5/1.02 mm,

septum 0.2 mm, World Precision Instruments, RRID:SCR_008593) using a PUL-100 micropipette puller (World Precision Instruments, RRID:SCR_008593) to a tip resistance of 4–6 MΩ). The glass pipettes were then filled with a NaCl (1 M) solution to act as a carrier of current and two silver electrodes, +/−, were inserted into the pipette. Identical to the field stimulation the preBötC was first identified as spontaneously rhythmically active, then brought to cessation (with low-aCSF, CPP, and NBQX), and the micropipette was inserted into the preBötC. Trains of bipolar pulses with constant current (interval: 20 ms, pulse duration: 2 ms, 80–100 μA), were used to stimulate fibers and neurons adjacent to the tip of the pipette with the same stimulation unit used for field stimulation. Both types of stimulus electrodes were guided visually to the desired region using a MPC-200 micromanipulator system (Sutter Instruments) under 10× and 40× magnification. In all stimulation experiments, the stimulation itself was applied 1.5 s after the optical recording had begun.

Drug application

Glutamatergic and GABAergic transmission was blocked using 20 μM NBQX disodium salt (AMPA receptor antagonist, Tocris Bioscience, catalog #1044, 20 mM stock, in H_2O, RRID:SCR_003689), 20 μM CPP (NMDA receptor antagonist, Tocris Bioscience, catalog #0173, 20 mM stock, in H_2O, RRID:SCR_003689), 1 μM strychnine (glycine receptor antagonist, Sigma-Aldrich, catalog #S8753, 1 mM stock, in H_2O, RRID:SCR_008988), and 20 μM gabazine ($GABA_A$ receptor antagonist, Sigma-Aldrich, catalog #505986, 20 mM stock, in H_2O, RRID:SCR_008988). In some experiments, 5 μM TFB-TBOA (a potent and selective glial glutamate transporter EAAT1 and EAAT2 inhibitor, Tocris Bioscience, catalog #2532, 1 mM stock, in DMSO, RRID:SCR_003689), was added to the recirculating aCSF. For puffing experiments the drugs used were: 1 μM TTX (Tocris Bioscience, catalog #1078, 3 mM stock, in H_2O, RRID:SCR_003689, bath applied), 1 mM glutamate (Sigma-Aldrich, Product number #G5889, 1 mM stock, in H_2O, RRID:SCR_008988), and 1 mM GABA (Sigma-Aldrich, Product number #A2129, 1 mM stock, in H_2O, RRID:SCR_008988). For DAMGO experiments, 1 μM DAMGO (selective MOR agonist, Tocris Bioscience, catalog #1171, 1 mM, in H_2O, RRID:SCR_003689) was added and in some of these experiments, cadmium sulfate 100 μM (Sigma-Aldrich, catalog #481882, 5 mM stock, in H_2O, RRID:SCR_008988) was used to block transmitter release.

Imaging of glutamate, GABA, and Ca^{2+}

Imaging of the glutamate/GABA sensors and GECIs was done using wide-field fluorescence on a fixed-stage upright microscope (modified Olympus BX51, RRID:SCR_018949), illuminated by a metal halide light source (PhotoFluor II, 89North) or a blue (470 nm) LED light source (M470L2, Thorlabs). Red and green channel fluorescence was visualized using a dual-bandpass filter set (Chroma 59022: excitation dual bandpass 450–490/555–590 nm, emission dual bandpass 500–543/603–665 nm). Time series acquisition was performed with a sCMOS camera (Neo DC-152Q, Andor Technology) controlled by SOLIS software (Andor Technology). SF-iGluSnFR.A184S was imaged with time-series of 50–400 frames at a frequency of 5–20 frames/s. iGABASnFR was imaged using time-series 30–200 frames at a frequency of 5–10 frames/s. Ca^{2+} (jGCaMP7f, jRCaMP1b) was imaged used time-series of 100–400 frames at a frequency of 5–10 frames/s. Imaging protocols employed 10× (NA 0.3), 20× (NA 0.5), 40× (NA 0.8), 63× (NA 0.95) water immersion objectives.

Experimental design and statistical analysis

Glutamate, GABA and Ca^{2+} transients were calculated as the percent change in fluorescence relative to baseline values ($\Delta F/F_0$). $\Delta F/F_0$ ($F1–F_0/F_0$) was calculated by setting F_0 as the baseline point just before a burst occurred and F1 as the peak of that same burst. For stimulus-induced transients F_0 was set as the minimal value just before the stimulation triggered response and F1 as the peak intensity. The intensity values used for the calculations were collected either as a summation of the entire field of view fluorescence using a rectangular region (referred to as a network-region of interest (ROI), sized from 395 × 395 pixels to 1245 × 1047 pixels, or from individual putative synapse-like structures using circular ROIs (referred to as synapse-ROIs) sized 10 × 10 pixels. When imaging the effect of DAMGO on spontaneous rhythmic activity a standard ROI of 640 × 520 pixels was used.

Optical data were analyzed offline using ImageJ 1.53d (ImageJ, RRID:SCR_003070), and Igor Pro 8 (IGOR Pro, RRID:SCR_000325). Electrophysiological data were acquired using pClamp 10.3 (pClamp, RRID:SCR_011323). All statistical tests and graphics were performed using GraphPad Prism 8 (GraphPad, RRID:SCR_002798). When relevant data were verified for normal distribution with Shapiro–Wilk test, then analyzed using one-way ANOVA with Tukey's *post hoc* test and unpaired and paired Student's *t* test both two and one-tailed. Some data were fitted to a nonlinear power function ($Y = A \times X^B + C \times X^D$). Results are, in the text, reported as mean ± standard deviation, and graphically as mean ± SEM; *N* = number of cultures, *n* = number of punctuate synapse-like structures, or spontaneous burst cycles. Statistical significance was set at $p = 0.05$ based on the culture number for system and neuronal activity data ($p > 0.05$ = ns, $^*p < 0.05$, $^{**}p < 0.01$, $^{***}p < 0.001$, $^{****}p < 0.0001$).

Results

Organotypic slice cultures of the brainstem containing the preBötC generate spontaneous bilateral synchronous network oscillations (Phillips et al., 2016), and the long-term culture conditions permit the use of adeno-associated viral techniques to express GECIs visualizing cellular, and subcellular Ca^{2+} transients during rhythmic activity (Phillips et al., 2018; Daniel Gómez et al., 2021). Here, we extended this culture system to express genetically-encoded sensors for glutamate and GABA to directly visualize the release of these transmitters in the preBötC.

Visualization of glutamatergic and GABAergic signaling in the rhythmic preBötC, using the glutamate and GABA sensors SF-iGluSnFR.A184S and iGABASnFR

Bilateral injections of the ventrolateral area of organotypic slice cultures with AAVRetro-SF-iGluSnFR.A184S, enabled imaging of spontaneous rhythmic glutamate transients in the preBötC. At low magnification Objective ((Obj.) 5–10×) the labeled preBötC was identifiable with clear neuronal labeling and rhythmic activity (Fig. 1*A*). High magnification (Obj. 40–63×) allowed for detailed imaging of the soma-dendritic regions of single SF-iGluSnFR.A184S-labeled neurons during rhythmic activity (Fig. 1*E*). It was evident that the release of glutamate had a punctate spatial distribution, appearing as small high-intensity areas on the soma and dendritic areas of the labeled neurons, and these "hotspots" of glutamatergic fluorescence signals are hypothesized to be putative glutamatergic synapses. To compare the bursting dynamics of the summed network and these individual putative glutamatergic synapses, the temporal kinetics of the fluorescence signal was analyzed using two types of ROIs. A network-ROI, which encompassed the entire preBötC, and a synapse-ROI, which only encompassed a single putative synapse (Fig. 1*A*). No significant difference was found between the frequency [network-ROI: 24 ± 11 burst/min, synapse-ROI: 27 ± 10 burst/min, unpaired Student's *t* test, $t_{(70)} = 1.05$, $p = 0.30$ (ns); Fig. 1*B*], the risetime [network-ROI: 0.28 ± 0.04 s, synapse-ROI: 0.29 ± 0.10 s, unpaired Student's *t* test, $t_{(67)} = 0.64$, $p = 0.52$ (ns); Fig. 1*B*], the halfwidth [network-ROI: 0.75 ± 0.29 s, synapse-ROI: 0.81 ± 0.35 s, unpaired Student's *t* test, $t_{(69)} = 0.81$, $p = 0.42$ (ns); Fig. 1*B*], or the decay time [network-ROI: 1.8 ± 1.0 s, synapse-ROI: 1.4 ± 1.2 s, unpaired Student's *t* test, $t_{(70)} = 1.45$, $p = 0.15$ (ns); Fig. 1*B*] of synapse-like structures and the summed network activity ($N = 37$, $n = 407$).

To confirm that SF-iGluSnFR.A184S specifically senses glutamate, 1 μM TTX was added to the aCSF to inhibit spontaneous

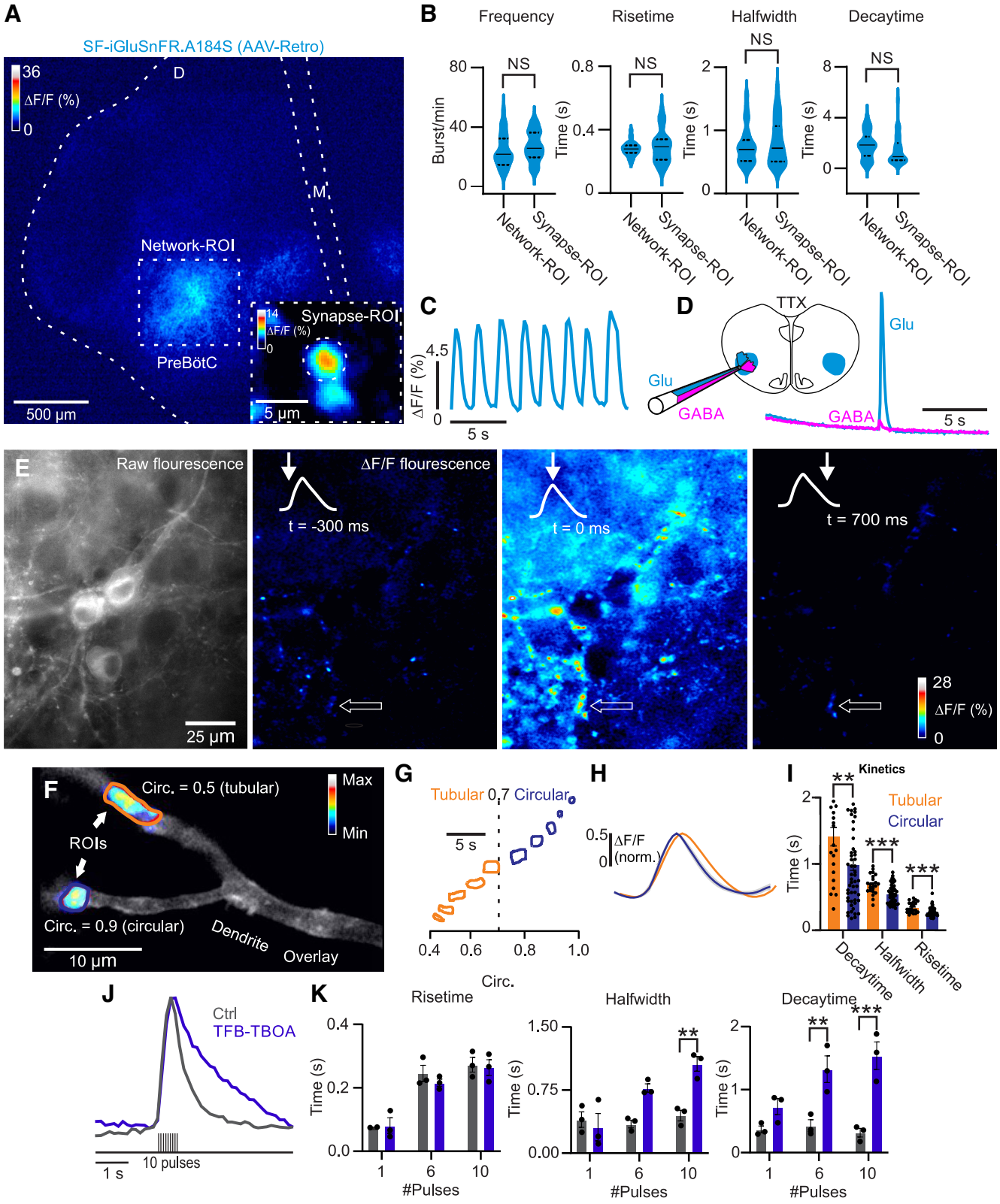

Figure 1. Visualization of glutamate transients during spontaneous rhythmic activity, using the glutamate sensor SF-iGluSnFR.A184S. ***A***, Cycle-triggered averaged image (9 cycles over a 20-s epoch) of the ΔF/F glutamate transients from a rhythmic slice culture, bilaterally injected with AAVRetro-SF-iGluSnFR.A184S. Dotted square represents a network-ROI encompassing the PreBötC. Bottom right corner, Cycle-triggered averaged image (11 cycles over a 40-s epoch) of the ΔF/F glutamate transients from a single punctuate synapse-like structure, imaged at higher magnification, with a representation of a synapse-ROI (dotted circle). ***B***, Left to right, Glutamate transient burst frequency, risetime, halfwidth, and decay time (median line and two quartile lines), all measured with both network ($N = 40$) and synapse-ROIs ($N = 37$, $n = 407$). ***C***, ΔF/F (%) from a network-ROI of the rhythmic preBötC seen in the image in panel ***A***. ***D***, Diagram of the experimental paradigm validating the sensitivity of SF-iGluSnFR.A184S, and effect of pressure application of 1 mM glutamate or 1 mM GABA onto SF-iGluSnFR.A184S-labeled neurons with TTX present. ***E***, Left to right, Raw fluorescence image showing neuronal labeling with SF-iGluSnFR.A184S. Next are three images, all cycle-triggered averages (11 cycles over a 40-s epoch), of ΔF/F glutamate transients, each image showing a different time relative to the peak of the averaged burst (1st: 300 ms before peak, 2nd: on peak, 3rd: 700 ms after peak, inset solid arrows).

rhythm and action potential-driven transmitter release, which was followed by pressure application of 1 mM glutamate or 1 mM GABA from a glass pipette placed near SF-iGluSnFR.A184S labeled cells. These experiments showed that SF-iGluSnFR.A184S has a high specificity toward glutamate over GABA ($N = 3$; Fig. 1*D*).

Putative glutamatergic synapses displayed two distinct morphologies

The spatial outline of "hotspot" glutamate transients located on labeled dendrites or somas had two distinct morphologic shapes, an elongated tubular and a circular round synapse-like shape (Fig. 1*F*). To discriminate between these two synapse-like shapes, ROIs were hand drawn around the boundary of the putative synapse and then grouped according to their calculated circularity. A circularity below 0.7 was classified as tubular and above 0.7 as circular (Fig. 1*G*). Tubular synapses displayed slower kinetics with increased decay time (tubular: 1.42 ± 0.65 s, circular: 0.99 ± 0.62 s, unpaired Student's *t* test, $t_{(75)} = 2.69$, $p = 0.0087$; Fig. 1*H*,*I*), halfwidth (tubular: 0.70 ± 0.15 s, circular: 0.55 ± 0.14 s, unpaired Student's *t* test, $t_{(75)} = 4.06$, $p = 0.0001$; Fig. 1*H*,*I*), and risetime (tubular: 0.35 ± 0.08 s, circular: 0.28 ± 0.07 s, unpaired Student's *t* test, $t_{(75)} = 3.80$, $p = 0.0003$; Fig. 1*H*,*I*, $N = 5$, $n = 22–55$).

TFB-TBOA prolonged the decay time and halfwidth but not the risetime of glutamate transients

To further investigate SF-iGluSnFR.A184S's sensitivity, the glutamate reuptake system in the preBötC was chemically inhibited by adding the potent glutamate reuptake inhibitor TFB-TBOA (5 μM) to the recirculating aCSF. After identifying spontaneous rhythmic activity in a culture, the rhythm was stopped by superfusion with low-aCSF, and by adding CPP (20 μM) and NBQX (20 μM).

A theta-glass pipette, placed in the preBötC, was then used to give microstimulation trains of 1, 6, and 10 electrical stimulus pulses to evoke glutamate transients. The kinetics of the resulting stimulus-induced glutamate transients were measured before and after adding TFB-TBOA. The control decay time, in reponse to stimulation with a train consisting of 10 pulses, was markedly increased when TFB-TBOA was added (one-way ANOVA, $F = 13.25$, Turkey's *post hoc* analysis, Ctrl. vs TFB-TBOA, $p = 0.0007$; Fig. 1*J*,*K*) and halfwidth (one-way ANOVA, $F = 10.42$, Turkey's *post hoc* analysis, Ctrl. vs TFB-TBOA, $p = 0.0052$; Fig. 1*J*,*K*), but not risetime [one-way ANOVA, $F = 15.63$, Turkey's *post hoc* analysis, Ctrl. vs TFB-TBOA, $p = 0.99$ (ns); Fig. 1*J*,*K*, $N = 3$, $n = 30$] of stimulus-induced glutamate transients.

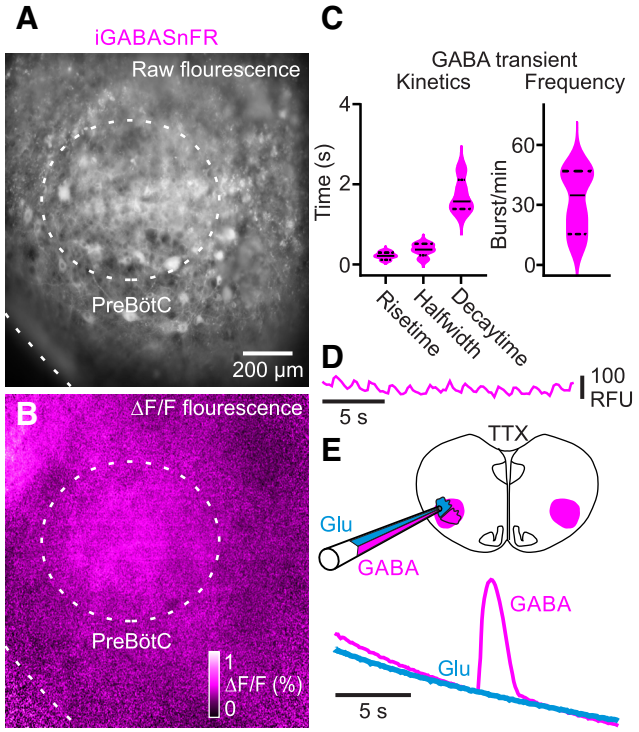

Figure 2. Visualization of GABA transients during spontaneous rhythmic activity, using the GABA sensor iGABASnFR. ***A***, Raw fluorescence image of a slice culture labeled with iGABASnFR, and a network-ROI encompassing the PreBötC (dotted circle). ***B***, Cycle-triggered averaged image (28 cycles over a 40-s epoch) of the ΔF/F GABA transients from same slice culture as in panel ***A***. ***C***, Spontaneous GABA transient risetime, halfwidth, and decay time (median line and two quartile lines), all measured with a network-ROI ($N = 40$). ***D***, Spontaneous GABA transients in the network-ROI from the rhythmic culture depicted in panel ***A***. ***E***, Diagram of the experimental paradigm validating the sensitivity of iGABASnFR, and effect of pressure application of 1 mM glutamate or 1 mM GABA onto iGABASnFR-labeled neurons with TTX present. Note that only application of GABA gives a noticeable florescence response.

Visualization of GABA transients with iGABASnFR had a diffuse and hazy appearance but still allowed temporal measurements of GABA dynamics

To investigate the dynamics of GABA release during spontaneous rhythmic activity in the preBötC, organotypic slice cultures were bilateral-injected with the AAV1-iGABASnFR in the ventrolateral area. Rhythmic GABA transients were observed and imaging of the raw fluorescence signal showed clearly identifiable neurons and processes (Fig. 2*A*,*D*). However, looking at the GABA dynamics over time, across multiple bursts (ΔF/F), the image did not have the same punctuate synapse-like appearance as the SF-iGluSnFR.A184S labeling, and presented with a hazy and more diffuse appearance (Fig. 2*B*). However, the fluorescence data acquired through a network-ROI was sufficient for analysis of the temporal kinetics underlying the summed preBötC GABA release dynamics (risetime: 0.22 ± 0.08 s, halfwidth: 0.37 ± 0.15 s, decay time: 1.70 ± 0.43 s; Fig. 2*C*), and burst frequency 32 ± 17 burst/min ($N = 5$). To also confirm that iGABASnFR specifically senses GABA, 1 μM TTX was added to the aCSF to inhibit spontaneous rhythm and action potential-driven transmitter release, which was followed by pressure application of 1 mM glutamate or 1 mM GABA from a

←

Notice the spatial resolution allows visualization of punctuate synapse-like glutamate "hotspots" (empty arrows). ***F***, High magnification of a preBötC dendrite overlaid with glutamate transients (color normalized), highlighting the different morphologies of the glutamatergic synapse-like structures (tubular and circular) that can be seen on dendritic profiles. ***G***, Examples of hand drawn ROIs, and their calculated circularity, with an arbitrary threshold set at circ. = 0.7 as the border between tubular and circular. ***H***, Averaged traces from all bursts of tubular and circular ROIs drawn from the data represented in ***G***. ***I***, Decay time, halfwidth and risetime (mean ± SEM) of glutamate transients from hand-drawn ROIs of both tubular (circ. < 0.7, $N = 7$, $n = 22$) and circular synapse-like structures (circ. > 0.7, $N = 9$, $n = 55$). ***J***, Network-ROI ΔF/F glutamate transients (in low-aCSF, with 20 μM NBQX + 20 μM CPP) from three stimulations in time epochs of 15 s with 10 pulses before and after addition of 5 μM TFB-TBOA. ***K***, Left to right, Stimulation triggered transients (1, 6, and 10 pulses) and their risetime, halfwidth, and decay time (mean ± SEM), before (gray bar) and after addition of 5 μM TFB-TBOA (blue bar, $N = 3$, $n = 30$).

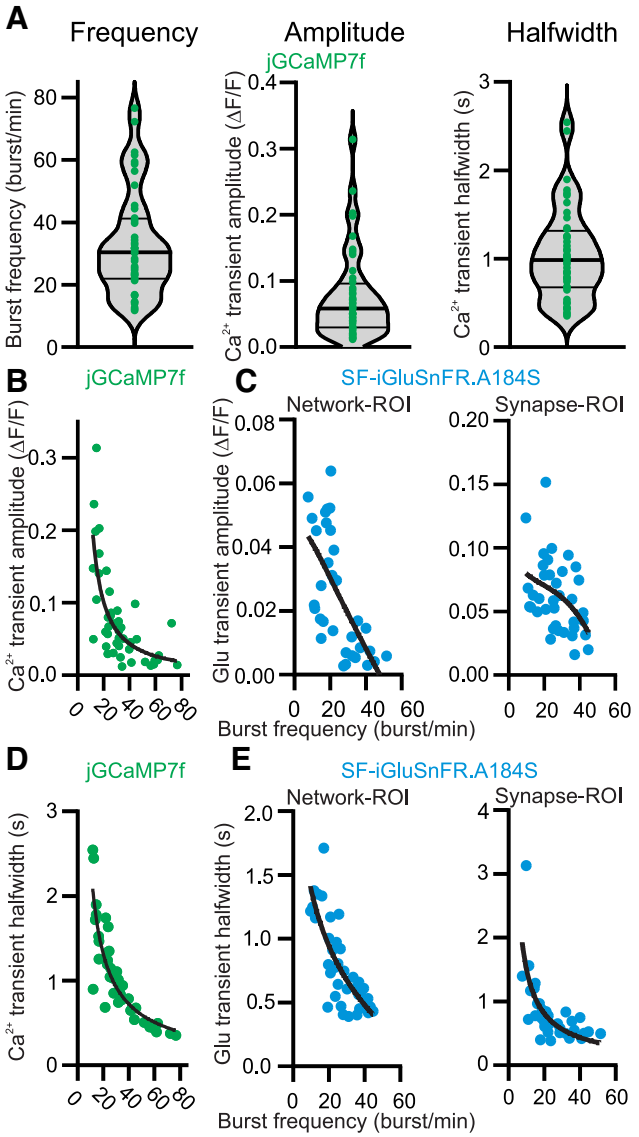

Figure 3. Relationship between burst frequency and amplitude, halfwidth of Ca^{2+} and glutamate transients. ***A***, Left to right, Violin plots (all data point and median line and two quartile lines) of spontaneous burst frequency, Ca^{2+} transient amplitudes (ΔF/F), and Ca^{2+} transient halfwidths (jGCaMP7f) from preBötC network-ROIs. ***B***, Relationship between burst frequency and Ca^{2+} transient amplitudes (black line is a nonlinear power function fit, as in ***C–E***). ***C***, Relationship between burst frequency and glutamate transient amplitudes (ΔF/F, SF-iGluSnFR.A184S) from network-ROIs ($N = 44$) and synapse-ROIs ($N = 37$, $n = 407$). ***D***, Relationship between burst frequency and Ca^{2+} transient halfwidths. ***E***, Relationship between burst frequency and glutamate transient halfwidths from network-ROIs ($N = 44$) and synapse-ROIs ($N = 37$, $n = 407$). Note the inverse relationship between burst frequency and transient amplitudes and halfwidths for both sensors.

glass pipette placed near iGABASnFR-labeled cells. These experiments showed that iGABASnFR has a high specificity toward GABA over glutamate ($N = 3$; Fig. 2*E*).

Relationship between burst frequency and amplitude, halfwidth of rhythmic Ca^{2+} and glutamate transients

Spontaneous rhythmic activity in the preBötC measured using jGCaMP7f had a burst frequency of 33 ± 17 burst/min, a Ca^{2+} transient amplitude of 0.08 ± 0.07 ΔF/F, and halfwidth of 1.05 ± 0.52 s ($N = 44$; Fig. 3*A*). Violin plots of these measurements showed a large variation around the mean. Thus, a given culture might have half or double the mean burst frequency of the entire sample of 44 cultures (Fig. 3*A*). To determine whether there was a relationship between the burst frequency and the amplitude and halfwidth of both Ca^{2+}- and glutamate transients (with SF-iGluSnFR.A184S data from both network-ROI and synapse-ROI) these variables were plotted against each other (Fig. 3*B–E*). Interestingly, rhythmic Ca^{2+} transients and glutamate transients had an inverse relationship between the spontaneous burst frequency and the amplitude fluorescence from the given sensor (Fig. 3*B*,*C*). This inverse relationship was also observed between the burst frequency and burst halfwidth of the Ca^{2+} and glutamate transients (Fig. 3*D*,*E*). Thus, as the burst frequency increase the corresponding burst amplitude and halfwidth decrease. This relationship did not present as grouped, but rather as a continuum.

DAMGO-induced changes in preBötC rhythm and Ca^{2+} transient amplitude

Double transduction with first AAVRetro-jGCaMP7f unilateral-injected in the right ventrolateral preBötC area, followed by drop transduction of the entire culture with AAV9-JRCaMP1b (Fig. 4*A*), permitted alternating dual-imaging (20 s jGCaMP7f imaging followed by 20 s JRCaMP1b imaging) of rhythmic Ca^{2+} transients in the retrogradely labeled contralateral preBötC area (JGCaMP7f, green fluorescence), and regions outside the preBötC (JRCaMP1b, red fluorescence). This dual-labeling approach permitted quantification of Ca^{2+} transient amplitudes in the core rhythmogenic preBötC area, and surrounding regions, whose activity presumable is driven by preBötC activity. Control images from a ROI encompassing the preBötC were compared with images after adding the MOR agonist DAMGO (1 μM for 15 min) to the standard aCSF (Fig. 4*B*). DAMGO reduced the burst frequency from 34 ± 8 to 20 ± 5 bursts/min, with a partial reversal of the effect after a 30-min wash (one-way ANOVA, $F = 34.65$, $p = 0.0002$, $N = 5$. Tukey's *post hoc* analysis of Ctrl. vs DAMGO-15 min, $p = 0.0038$, DAMGO-15 min vs wash, $p = 0.018$; Fig. 4*C*). Interestingly, the Ca^{2+} transient amplitudes were increased by DAMGO measured with both jGCaMP7f and JRCaMP1b in the contralateral preBötC area. jGCaMP7f: Ctrl., 12.2 ± 12.6 ΔF/F %, DAMGO-15 min, 21.4 ± 19.1 ΔF/F % (ratio paired Student's *t* test, $t_{(5)} = 3.92$, $p = 0.0052$, $N = 6$). JRCaMP1b: Ctrl., 10.4 ± 4.2 ΔF/F %, DAMGO-15 min, 11.9 ± 4.1 ΔF/F % (ratio paired Student's *t* test, $t_{(5)} = 3.33$, $p = 0.0104$, $N = 6$). The Ca^{2+} transient halfwidths were increased from 765 ± 205 to 946 ± 280 ms (paired Student's *t* test, $t_{(5)} = 2.83$, $p = 0.01$, $N = 5$). Rhythmic Ca^{2+} transient amplitudes (JRCaMP1b) outside the preBötC in a combined region encompassing pre-XII, XII, and para-medial regions did not change. Ctrl., 8.8 ± 3.1 ΔF/F %, DAMGO-15 min, 7.7 ± 2.7 ΔF/F % (ratio paired Student's *t* test, $t_{(5)} = 1.82$, $p = 0.063$ (ns), $N = 6$). Thus, a 15-min application of DAMGO resulted in the predicted reduction in the spontaneous rhythmic preBötC activity (Ramirez et al., 2021), which was accompanied by an increased amplitude of the Ca^{2+} transients coming from the combined ensemble of neurons in the preBötC.

Hypoxia-induced changes in preBötC rhythm and Ca^{2+} transients did not display an inverse relationship between the burst frequency and rhythmical Ca^{2+} transients

To determine whether a reduction in burst frequency, brought about by pharmacological perturbation of rhythmic processes in the preBötC, is always accompanied by an increase in the amplitude of the Ca^{2+} transients coming from preBötC neurons, slice cultures were exposed to a hypoxic insult (Fig. 5). Control images

from a ROI encompassing the preBötC were compared with images after 30-min hypoxia induced by changing the standard aCSF to an aCSF solution prebubbled with 95% N_2/5% CO_2 (Fig. 5*A*). Hypoxia reduced the burst frequency from 36 ± 8 to 15 ± 6 bursts/min (paired Student's *t* test, $t_{(5)} = 5.97$, $p = 0.0009$, $N = 6$). However, the Ca^{2+} transient amplitudes were reduced by hypoxia measured with both jGCaMP7f and JRCaMP1b in the contralateral preBötC. jGCaMP7f: Ctrl., 13.7 ± 7.1 ΔF/F %, hypoxia-30 min, 7.7 ± 4.9 ΔF/F % (paired Student's *t* test, $t_{(5)} = 3.82$, $p = 0.005$, $N = 6$). JRCaMP1b: Ctrl., 16.8 ± 8.0 ΔF/F %, hypoxia-30 min, 7.5 ± 4.5 ΔF/F % (paired Student's *t* test, $t_{(5)} = 4.78$, $p = 0.003$, $N = 6$). Rhythmic Ca^{2+} transients (JRCaMP1b) outside the preBötC in a combined region encompassing pre-XII, XII, and para-medial regions were also reduced by hypoxia: Ctrl., 18.9 ± 10.1 ΔF/F %, hypoxia-30 min, 3.3 ± 2.8 ΔF/F % (paired Student's *t* test, $t_{(5)} = 4.38$, $p = 0.004$, $N = 6$). The Ca^{2+} transient halfwidths (jGCaMP7f) were reduced from 595 ± 176 to 416 ± 38 ms (paired Student's *t* test, $t_{(4)} = 2.75$, $p = 0.03$, $N = 5$). Interestingly, although the general effect of hypoxia was a reduction in Ca^{2+} transient amplitudes in larger regions sampled in the culture, cellular level imaging revealed that a subset of neurons in and around the preBötC showed an increase in Ca^{2+} transient amplitude of 5.8 ± 3.9% ΔF/F ($N = 5$, $n = 49$ neurons) in response to hypoxia (Fig. 5*D*).

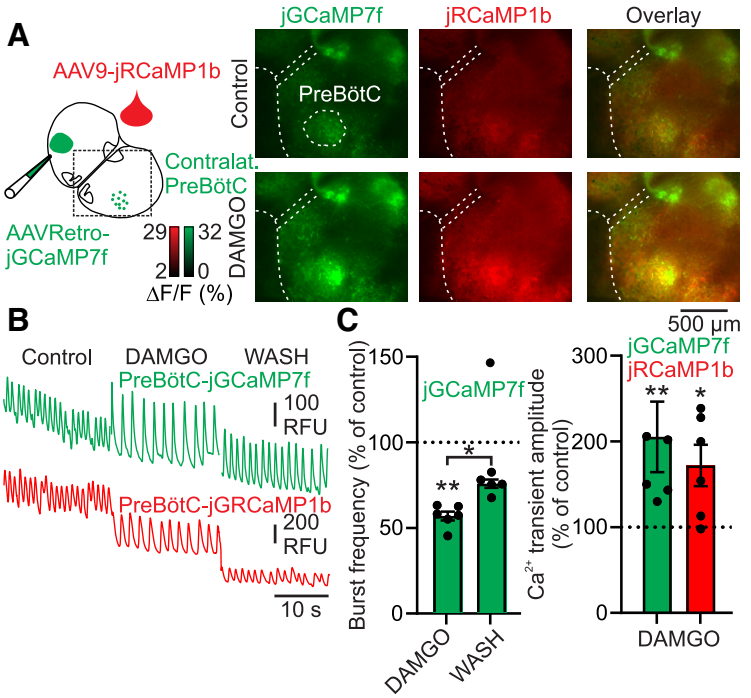

Figure 4. DAMGO reduces burst frequency, but increases Ca^{2+} transient amplitudes. ***A***, Left panel, Diagram of the experimental paradigm. Organotypic slice cultures containing the preBötC were injected with AAVRetro-jGCaMP7f in the right ventrolateral area, followed by drop-transduction with AAV9-jRCaMP1b (1 d later). After 7–14 d, rhythmic activity in the left side of the culture (dotted square) was imaged while exciting jGCaMP7f and jRCaMP1b in tandem (20-s epochs). Right panels, Cycle-triggered averaged images (3–15 cycles over 20-s epochs) of the Ca^{2+} transients for jGCaMP7f (green), jRCaMP1b (red), and overlay, under control and after 15 min of 1 µM DAMGO. ***B***, Raw fluorescence traces (RFU: relative fluorescence units) from a ROI encompassing the preBötC (dotted square in ***A***, Control-jGCaMP7f) in the jGCaMP7f (green) and jRCaMP1b (red) imaging channels in control, during 15 min of DAMGO, and after a 30-min wash. Note the decrease in burst frequency, but increase in Ca^{2+} transient amplitudes. ***C***, Group data (mean ± SEM) of the burst frequency and Ca^{2+} transient amplitude response to DAMGO in the respective fluorescence channels.

DAMGO-induced changes in glutamate and GABA transients during spontaneous preBötC rhythm

To determine the effect of DAMGO on the amplitude of glutamate and GABA transients during spontaneous rhythmic activity, imaging was performed from network-ROIs placed in the preBötC in SF-iGluSnFR.A184S or iGABASnFR-labeled slice cultures (Fig. 6). In SF-iGluSnFR.A184S-labeled cultures, application of DAMGO reduced the burst frequency from 36 ± 7 burst/min (Ctrl.) to 20 ± 2 burst/min (DAMGO-15 min) and 25 ± 3 burst/min (DAMGO-30 min), with a partial reversal of the effect after a 30-min wash [Ctrl. vs DAMGO-15 min: paired Student's *t* test, $t_{(3)} = 4.97$, $p = 0.0078$, Ctrl. vs DAMGO-30 min: paired Student's *t* test, $t_{(3)} = 5.61$, $p = 0.0056$, Ctrl. vs wash-30 min: paired Student's *t* test, $t_{(3)} = 2.22$, $p = 0.057$ (ns), $N = 4$; Fig. 6*B*]. The same effect was observed in iGABASnFR-labeled cultures, where application of DAMGO for 15 and 30 min reduced burst frequency from 32 ± 17 burst/min (Ctrl.) to 17 ± 10 burst/min (DAMGO-15) and 22 ± 5 burst/min (DAMGO-30), respectively. A reversal of the effect was also observed after washing for 30 min, increasing the burst frequency to 30 ± 12 burst/min [Ctrl. vs DAMGO-15 min: paired Student's *t* test, $t_{(3)} = 3.55$, $p = 0.019$, Ctrl. vs DAMGO-30 min: paired Student's *t* test, $t_{(2)} = 3.81$, $p = 0.031$, Ctrl. vs wash-30 min: paired Student's *t* test, $t_{(3)} = 0.87$, $p = 0.224$ (ns), $N = 4$; Fig. 6*D*]. Notably, application of DAMGO increased the amplitude of both rhythmic glutamate and GABA transients. In SF-iGluSnFR.A184S-labeled cultures, application of DAMGO for 15 min, but not 30 min, increased the glutamate transient amplitude to 166 ± 27 ΔF/F % relative to the control, with a reversal of the effect after a 30-min wash [Ctrl. vs DAMGO-15 min: 0.02 ± 0.01 (RFU) vs 0.03 ± 0.02 (RFU), paired Student's *t* test, $t_{(3)} = 2.61$, $p = 0.0396$, Ctrl. vs DAMGO-30 min: 0.02 ± 0.01 (RFU) vs 0.02 ± 0.02 (RFU), paired Student's *t* test, $t_{(3)} = 0.10$, $p = 0.46$ (ns), Ctrl. vs wash-30 min: 0.02 ± 0.01 (RFU) vs 0.02 ± 0.01 (RFU), paired Student's *t* test, $t_{(3)} = 0.05$, $p = 0.48$ (ns), $N = 4$; Fig. 6*A*,*B*]. In iGABASnFR-labeled cultures application of DAMGO for 15 min, but not 30 min, also increased the GABA transient amplitude to 282 ± 41 ΔF/F % relative to the control, with a reversal of the effect after a 30-min wash [Ctrl. vs DAMGO-15 min: 0.0018 ± 0.0004 (RFU) vs 0.005 ± 0.001 (RFU), paired Student's *t* test, $t_{(3)} = 8.33$, $p = 0.0018$, Ctrl. vs DAMGO-30 min: 0.0018 ± 0.0004 (RFU) vs 0.0042 ± 0.0019 (RFU), paired Student's *t* test, $t_{(3)} = 2.14$, $p = 0.061$ (ns), Ctrl. vs wash 30 min: 0.0018 ± 0.0004 (RFU) vs 0.0226 ± 0.0005 (RFU), paired Student's *t* test, $t_{(3)} = 1.89$, $p = 0.078$ (ns), $N = 4$; Fig. 6*C*,*D*].

DAMGO-induced changes in glutamate but not GABA signaling during stimulus-induced release under rhythm blockade

To determine whether DAMGO has an effect on glutamate and GABA release a series of experiments using a constant electrical field-stimulus to evoke glutamate and GABA transients were performed (Fig. 7). To begin, spontaneous rhythmic activity was brought to cessation using a cocktail of ionotropic ion channel blockers consisting of 20 µM NBQX, 20 µM CPP, 20 µM gabazine, and 1 µM strychnine, effectively blocking AMPA, NMDA,

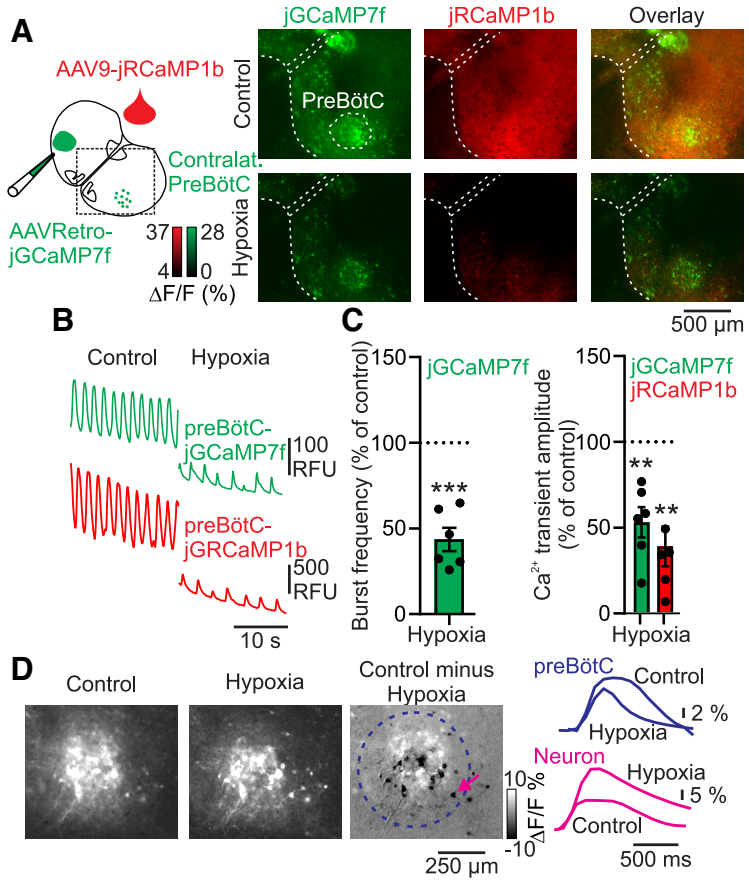

Figure 5. Hypoxia reduces both burst frequency and Ca^{2+} transient amplitudes. ***A***, Left panel, Diagram of the experimental paradigm. Organotypic slice cultures containing the preBötC were injected by AAVRetro-jGCaMP7f in the right ventrolateral area, followed by drop-transduction with AAV9-jRCaMP1b (1 d later). After 7–14 d, rhythmic activity in the left side of the culture (dotted square) was imaged exciting jGCaMP7f and jRCaMP1b in tandem (20-s epochs). Right panels, Cycle-triggered average images (3–15 cycles over 20-s epochs) of the ΔF/F Ca^{2+} transients for jGCaMP7f (green), jRCaMP1b (red), and overlay, under control and during 30-min hypoxia. ***B***, Raw fluorescence traces (RFU: relative fluorescence units) from a ROI encompassing the preBötC (dotted square in ***A***, Control-jGCaMP7f) in the jGCaMP7f (green) and jRCaMP1b (red) imaging channels in control, and after 30-min hypoxia. Note the decrease in burst frequency and Ca^{2+} transient amplitudes. ***C***, Group data (mean ± SEM) of the burst frequency and Ca^{2+} transient amplitude response to hypoxia in the respective fluorescence channels. ***D***, Left panel, Zoom of the preBötC area in control, and hypoxia imaged using jGCaMP7f. A digital subtraction of the two images (Control minus hypoxia) with contrast centered on zero, and max = 10, min = −10 ΔF/F % depicts neurons with a decrease in ΔF/F as white, and cells with an increase as black (example neuron: magenta arrow). Right panel, Top blue traces are cycle-triggered averages of Ca^{2+} transients in a ROI (blue dotted circle) encompassing the entire preBötC region in control and during hypoxia. Bottom magenta traces are cycle-triggered averages of Ca^{2+} transients in a ROI (magenta arrow) from a single neuron in the preBötC region. Note, that there are several neurons that show an increase in fluorescence, although the entire region on average shows a decrease.

$GABA_A$, and glycine receptors, respectively (Fig. 7*A*). This cocktail had two primary functions. First, it blocked spontaneous rhythmic activity, and ensured that following an electrical stimulation, activated neurons would not subsequently excite other preBötC neurons, which would invalidate quantification of the stimulus-induced glutamate and GABA release. Second, we rationalized that by blocking the major target receptors of glutamate and GABA most of the presynaptically released transmitter would bind to the optical sensor molecules, and the recorded signal would reflect the amount of transmitter released (Fig. 7*A*). Following the addition of the cocktail, a series of 16 preBötC field stimulations (train of 10 pulses, which was near maximal effect of trains; Fig. 7*F*) with 2-min intervals were conducted in one side of bilaterally AAV-injected cultures, without adding DAMGO to measure the baseline release of glutamate or GABA over time in a preBötC network-ROI (Fig. 7*C–E*). The field-stimulus electrode was then moved to the contralateral preBötC, and the stimulus paradigm was repeated with bath application of DAMGO after 8 min (Fig. 7*C*,*E*, solid arrow). The continuous stimulations (16), without application of DAMGO, showed a decrease in stimulus-induced glutamate and GABA transient amplitude over the entire ~20-min experiment, but the initial four to five stimulus showed minimal reductions. Importantly, DAMGO reduced the peak amplitude of the stimulus-induced glutamate transients, causing, in cumulated amplitudes ΔF/F of six, eight and 10 min after adding DAMGO, a decrease from 99.34 ± 0.03 ΔF/F % (relative to 1st four stimulations) to 57.94 ± 0.08 ΔF/F % (relative to 1st four stimulations; Ctrl. vs DAMGO cumulated amplitudes of 6-, 8-, and 10-min stimulations: paired Student's *t* test, $t_{(11)} = 13.99$, $p < 0.0001$, $N = 4$; Fig. 7*B*,*C*]. Next, the same experiment was performed with iGABASnFR (Fig. 7*E*), but here DAMGO did not change the amplitude of the stimulus-induced GABA transient [Ctrl. vs DAMGO cumulated amplitudes of 6-, 8-, and 10-min stimulations: 64.68 ± 40.29 ΔF/F % (relative to 1st four stimulations) vs 73.7 ± 38.7 ΔF/F % (relative to 1st four stimulations), paired Student's *t* test, $t_{(8)} = 0.61$, $p = 0.5542$ (ns), $N = 3$; Fig. 7*E*].

Discussion

In this study, we used genetically-encoded sensors to visualize the dynamics of Ca^{2+}, glutamate, and GABA in the rhythmic preBötC. There was inverse relationship between the spontaneous preBötC burst frequency and amplitude/halfwidth, appearing in the Ca^{2+} and glutamate signals. This inverse relationship was also noted when applying DAMGO, that slowed the rhythm, and increased burst amplitude/halfwidth. A hypoxic insult slowed the rhythm, but did not result in the same inverse relationship. Using electrical stimulus-evoked glutamate and GABA transients under rhythm-blockade, we found that DAMGO inhibits glutamate, but not GABA release. This indicates that MOR mediated slowing of the inspiratory rhythm involves inhibition of glutamate release, which would change the network dynamics, and impact the ability of glutamatergic neurons to engage in recurrent excitation affecting rhythmogenesis.

Visualization of glutamate and GABA in the preBötC

Using SF-iGluSnFR.A184S and iGABASnFR we optically confirm the involvement of glutamatergic and GABAergic signaling in the rhythmic preBötC (Del Negro et al., 2018; Ramirez and Baertsch, 2018). It is unclear whether SF-iGluSnFR.A184S is present in the presynaptic or postsynaptic membrane or both. The pattern of baseline labeling often included clear somatic and dendritic profiles, on top of which oscillating synapse-like areas were present, suggesting a postsynaptic expression. When the

frequency and kinetics of these individual putative synapses were compared with those of the summed network glutamate release, no significant difference was observed. From this, we rationalized that a network-ROI, encompassing the preBötC, would be representative of the underlying synaptic dynamics. The putative glutamatergic synapses had either an elongated tubular shape, or a round shape, with tubular synapses giving rise to kinetically slower glutamate transients. This difference could be a result of distinct glutamate clearance mechanisms giving rise to a spillover phenomenon at certain synapses in the network, or be labeled adjacent synapses along the dendrites. Time-lapse visualization of glutamatergic synapses in this organotypic culture system might permit studies that determine the stability or structural transformation of preBötC synapses during, e.g., hypoxic and pharmacological challenges.

In this study, we also visualized the GABA dynamics during rhythmic activity, but iGABASnFR did not have the same spatial punctate synapse-like appearance as SF-iGluSnFR.A184S. This could be because of different viral serotypes, since AAVRetro-SF-iGluSnFR.A184S was a retrograde virus whereas the AAV1-iGABASnFR was an AAV1, and we have noticed differences in subcellular expression and spatial distribution using the retrograde and AAV9 serotypes (Daniel Gómez et al., 2021). The release of GABA may also be less punctate because of differences in uptake mechanisms or synaptic arrangements in the preBötC.

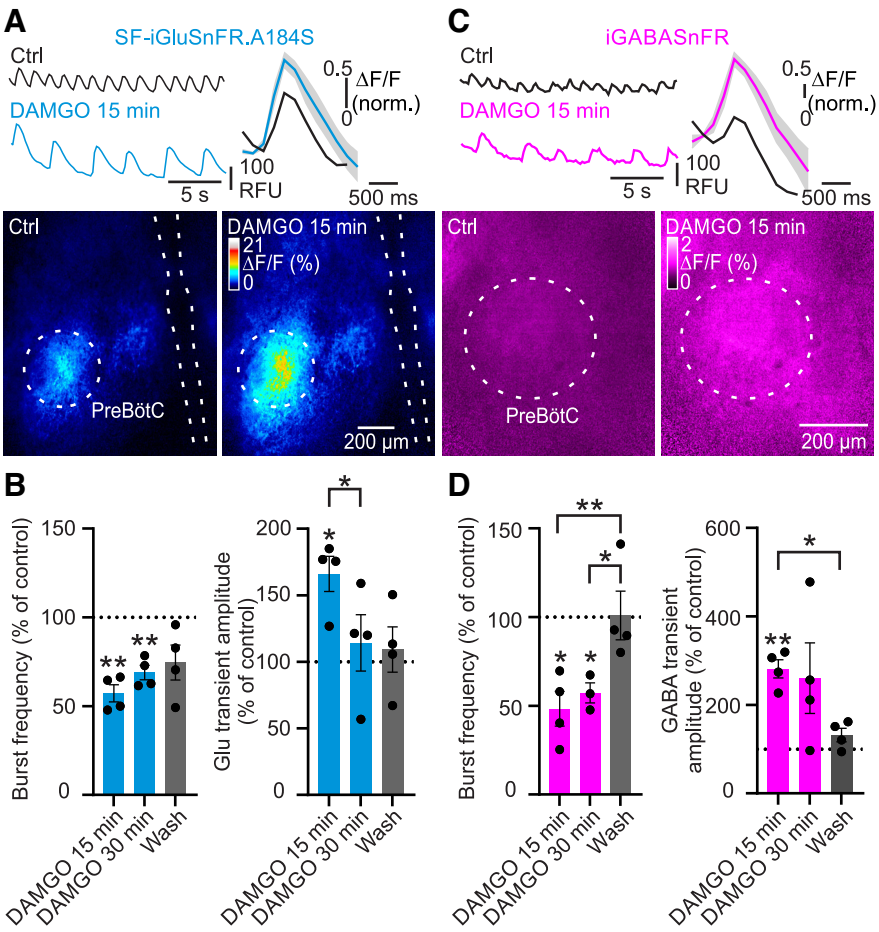

Figure 6. DAMGO-induced changes in glutamate and GABA signaling during spontaneous preBötC rhythm. ***A***, Top left, Raw fluorescence traces (SF-iGluSnFR.A184S; RFU: relative fluorescence units) from a network-ROI of the preBötC before and after 15-min addition of 1 μM DAMGO. Top right, Cycle-triggered averaged traces of glutamate transients before (Ctrl.) and after addition of 1 μM DAMGO (gray outlines are SEM error bands), normalized to Ctrl. ($N = 4$, Ctrl.: $n = 91$, DAMGO: $n = 53$). Bottom images, Cycle-triggered averaged images of the glutamate transients ($\Delta F/F$) before (27 cycles over a 40-s epoch) and after addition of 1 μM DAMGO (13 cycles over a 40-s epoch). ***B***, Group data (mean ± SEM) of the relative change in burst frequency (left) and glutamate transient amplitude (right) from control, at 15 and 30 min into 1 μM DAMGO and a 30-min wash, respectively ($N = 4$). ***C***, Top left, Raw fluorescence traces (iGABASnFR; RFU: relative fluorescence units) from a network-ROI of the preBötC before and after addition of 1 μM DAMGO. Top right, Cycle-triggered averaged traces of GABA transients before and after addition of 1 μM DAMGO (gray outlines are SEM error bands) normalized to Ctrl. ($N = 4$, Ctrl.: $n = 86$, DAMGO: $n = 53$). Bottom images, Cycle-triggered averaged images of the GABA transients before (28 cycles over a 40-s epoch) and after addition of 1 μM DAMGO (11 cycles over a 40-s epoch). ***D***, Group data (mean ± SEM) of the relative change in burst frequency (left) and GABA transient amplitude (right) from control, at 15 and 30 min into 1 μM DAMGO and a 30-min wash, respectively ($N = 4$). Note that both glutamate and GABA transients increase in amplitude during 15-min DAMGO, while burst frequency is reduced.

Inverse relationship between preBötC burst frequency and burst amplitude/halfwidth

The inverse relationship between burst frequency and burst amplitude/halfwidth was initially observed using the Ca^{2+} sensor jGCaMP7f, and suggests that a slower rhythm is associated with ensembles of preBötC neurons that spike more during a burst. The slower rhythm may also provide more time and baseline hyperpolarization to de-inactivate Ca^{2+} channels to a greater extent, and also de-inactivate more Na^{+} channels to cause higher amplitude spikes that evoke more Ca^{2+} channel activation. This would imply that stronger bursts should lead to an increase in glutamate release, which indeed was the case, as we observed the same inverse relationship when analyzing rhythmic glutamate transients. A number of studies have observed this inverse relationship using recordings from preBötC neurons, where inspiratory bursts are followed by afterhyperpolarizations, the size of which depend on the burst amplitude. Afterhyperpolarizations are likely because of intrinsic membrane properties, which in combination with a short period of synaptic depression cause a refractory period (Rekling et al., 1996; Zavala-Tecuapetla et al., 2008; Krey et al., 2010; Zhang et al., 2010; Picardo et al., 2013; Guerrier et al., 2015; Kottick and Del Negro, 2015; Baertsch et al., 2018; Revill et al., 2021). This would imply that weaker bursts should be followed by shorter refractory periods, and in support of this idea, phasic optogenetic stimulation of inhibitory neurons in the preBötC inhibit the excitatory drive during an ensemble burst causing an increase in burst frequency (Cregg et al., 2017; Baertsch et al., 2018). Together, these data suggest that the preBötC network sustains bursting with varying degree of ensemble activity, either through variation in number of spikes per burst, or number or type of participating neurons, thereby determining the length of the refractory period. Other factors must also be involved, since the respiratory network in the brainstem can sustain rhythmic motor output (on XII

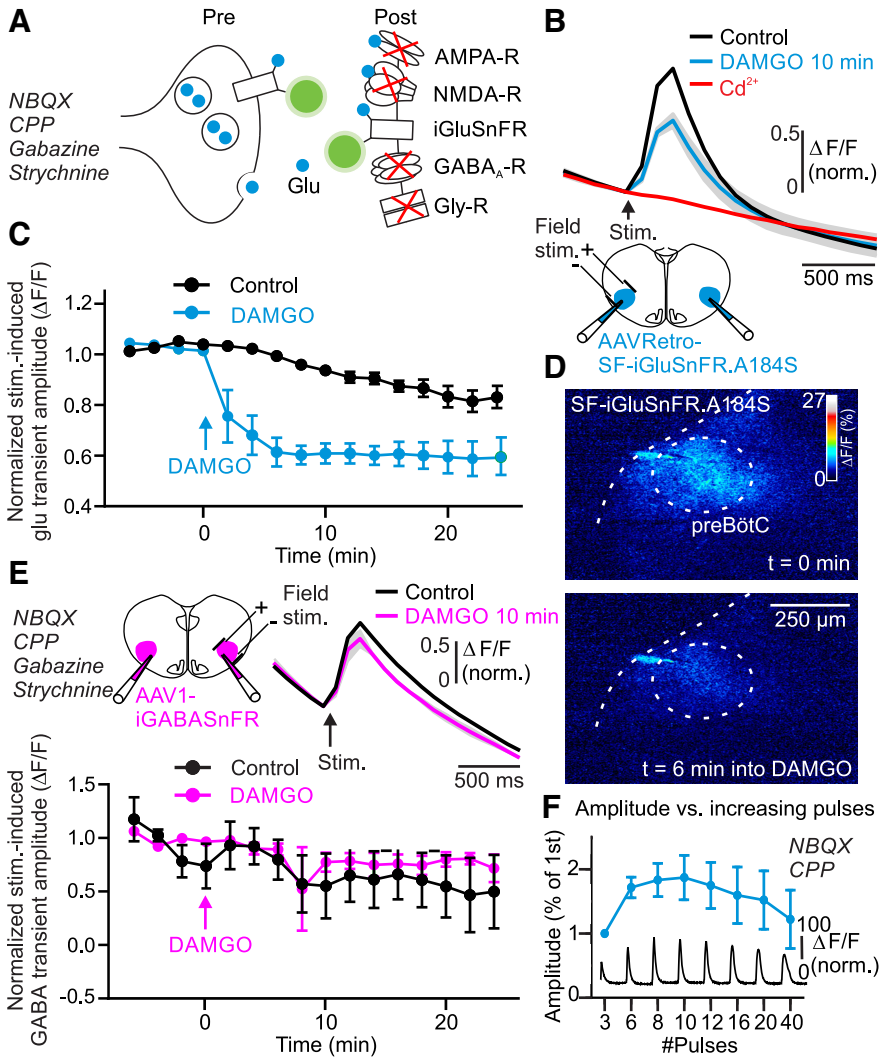

Figure 7. DAMGO-induced changes in glutamate, but not GABA signaling, during electrical stimulus-induced release under rhythm blockade. ***A***, Diagram illustrating how a cocktail of ion channel blockers (20 μM NBQX, 20 μM CPP, 20 μM gabazine, and 1 μM strychnine) is hypothesized to isolate SF-iGluSnFR.A184S as target for presynaptic release of glutamate. ***B***, Top, Averaged traces of stimulus-induced glutamate transients (normalized to 1st stimuli) before and after application of 1 μM DAMGO (10 min, gray outlines are SEM error bands) as well as after adding 100 μM cadmium sulfate (Cd^{2+}) to block all release ($N = 4$). Bottom, Diagram of the experimental paradigm for stimulus-induced glutamate transients. ***C***, Group data (mean ± SEM) of the normalized stimulus-induced glutamate transients over time (2-min intervals), with and without adding DAMGO ($N = 4$). ***, statistical significance for Ctrl. versus DAMGO cumulated amplitudes of 6, 8, and 10 min of stimulation. ***D***, Cycle-triggered averaged image of stimulus-induced glutamate transients (ΔF/F) before ($t = 0$ min) and 6 min into 1 μM DAMGO. ***E***, Top left, Diagram of the experimental paradigm of stimulus-induced GABA transients. Top right, Averaged traces of stimulus-induced GABA transients before and after application of 1 μM DAMGO (10 min, gray outlines are SEM error bands). Bottom, Group data (mean ± SEM) of the normalized stimulus-induced GABA transients over time (2-min intervals), with and without adding DAMGO ($N = 4$). ***F***, Relationship between amplitude of stimulus-induced glutamate transients and pulse numbers (peak amplitude normalized to 1st stimuli, $N = 5$). Note that DAMGO reduces the amplitude of stimulus-induced glutamate transients but has no effect on stimulus-induced GABA transients, suggesting an effect on presynaptic release of glutamate.

nerves) with similar amplitudes at very different frequencies (Del Negro et al., 2009).

Opioid-mediated changes in preBötC rhythm and glutamate release

That DAMGO-induced slowing of rhythmic preBötC activity is accompanied by an increase in burst amplitude/halfwidth in the organotypic cultures is surprising. Some in vitro studies on the isolated preBötC report no effect on the preBötC burst amplitude by MOR agonists (Sun et al., 2019, Wei and Ramirez, 2019), some report a decrease (Baertsch et al., 2021), some variable increase/decrease (Johnson et al., 1996; Burgraff et al., 2021), and some an increase (Barnes et al., 2007). We speculate that differences in preparation, concentration of the MOR agonists, and time dependency of the drug application might have captured different aspects of the MOR agonist response in these and our study.

Using dual-imaging (jGCaMP7f/JRCaMP1b) of rhythmic Ca^{2+} transients from the preBötC, and the surrounding rhythmic regions, we observed an increase in burst amplitude in the preBötC, but interestingly not in the surrounding regions, in response to DAMGO. However, both areas showed a reduced burst amplitude and more irregular rhythm during the hypoxic challenge. We hypothesize, that although both DAMGO and hypoxia lead to a reduced burst frequency, the underlying mechanisms might be different, with MOR activation being accompanied by burst amplitude increase in the core rhythmogenic preBötC. This idea is further supported by the observation that hypoxia, but not DAMGO, induces a subset of neurons in preBötC, which show an apparent increase in Ca^{2+} transient amplitude, while the overall effect is to decrease Ca^{2+} transient spontaneous rhythmic glutamate. The inverse relationship between burst frequency and burst amplitude/halfwidth in response to DAMGO was also observed when measuring glutamate and GABA transients, indicating that the slower rhythm indeed involves a phasic increase in glutamate and GABA release.

MOR agonists postsynaptically hyperpolarize preBötC neurons (Gray et al., 1999; Haji et al., 2003; Montandon et al., 2016; Baertsch et al., 2021), and electrophysiological experiments suggest that presynaptic release mechanisms are also involved (Takeda et al., 2001; Wei and Ramirez, 2019; Baertsch et al., 2021). Our optical measurements of glutamate release, under rhythm blockade, demonstrate that DAMGO indeed reduces the release of glutamate, but not GABA. It should be mentioned that this experimental paradigm is an indirect measurement of glutamate/GABA release, and there are some caveats. We surmise that the electrical stimulation using a stimulus train, recruits the same number of neurons/fibers before and after adding DAMGO, but do not know whether the hyperpolarizing action of DAMGO might cause some neurons to fail to be recruited. The glutamate and GABA signal is likely coming from other neurons in the preparation, but we cannot exclude that the electrical stimulus might have a releasing effect of glia cells, nor that metabotropic signaling might be involved as the cocktail only included

ionotropic blockers. The marked DAMGO effect on overall glutamate release in the preBötC is surprising, since only ~8% of preBötC neurons express MOR (Hayes et al., 2017; Bachmutsky et al., 2020), which may suggest that this small population of neurons have extensive glutamatergic connections within the preBötC.

How does the DAMGO-evoked presynaptic inhibition of glutamate release, but not GABA release, lead to a network effect that encompasses a larger burst amplitude/halfwidth of both intracellular Ca^{2+}, glutamate, and GABA transients? Our experiments do not point to a clear answer to this. One possibility is disinhibition, where reduced glutamate release lead to reduced excitation of a subset of inhibitory neurons, whereby inhibition is removed from part of the network leading to an overall increase in ensemble activity. An alternative is that the dynamics of the SF-iGluSnFR.A184S and iGABASnFR signals might change as the rhythm slow down. Sniffer-patch techniques might help solve this issue, more directly measuring glutamate release (Maeda et al., 1995).

Substance P, which increases rhythmic activity (Gray et al., 1999), appear to mediate this effect by affecting primarily the percolating phase leading up to a burst, without affecting the refractory period or burst duration (Baertsch and Ramirez, 2019). Thus, a picture emerges that different modulators of breathing frequency make use of different cellular mechanisms, and although the mechanisms at receptor and effector level are fairly well understood, the picture at the network level is still unclear, underscoring the need for unraveling the precise connectivity pattern among excitatory and inhibitory neurons in the preBötC.

In conclusion, opioid mediated slowing of preBötC rhythm involves presynaptic reduction of glutamate release, which may lead to changes in the network dynamics of both glutamatergic and GABAergic signaling.

References

Bachmutsky I, Wei XP, Kish E, Yackle K (2020) Opioids depress breathing through two small brainstem sites. Elife 9:e52694.

Baertsch NA, Ramirez JM (2019) Insights into the dynamic control of breathing revealed through cell-type-specific responses to substance P. Elife 8: e51350.

Baertsch NA, Baertsch HC, Ramirez JM (2018) The interdependence of excitation and inhibition for the control of dynamic breathing rhythms. Nat Commun 9:843.

Baertsch NA, Bush NE, Burgraff NJ, Ramirez JM (2021) Dual mechanisms of opioid-induced respiratory depression in the inspiratory rhythm-generating network. Elife 10:e67523.

Barnes BJ, Tuong CM, Mellen NM (2007) Functional imaging reveals respiratory network activity during hypoxic and opioid challenge in the neonate rat tilted sagittal slab preparation. J Neurophysiol 97:2283–2292.

Bodnar RJ (2022) Endogenous opiates and behavior: 2020. Peptides 151:170752.

Bouvier J, Thoby-Brisson M, Renier N, Dubreuil V, Ericson J, Champagnat J, Pierani A, Chédotal A, Fortin G (2010) Hindbrain interneurons and axon guidance signaling critical for breathing. Nat Neurosci 13:1066–1074.

Burgraff NJ, Bush NE, Ramirez JM, Baertsch NA (2021) Dynamic rhythmogenic network states drive differential opioid responses in the in vitro respiratory network. J Neurosci 41:9919–9931.

Chevalier M, De Sa R, Cardoit L, Thoby-Brisson M (2016) Mechanisms underlying adaptation of respiratory network activity to modulatory stimuli in the mouse embryo. Neural Plast 2016:1–10.

Cregg JM, Chu KA, Dick TE, Landmesser LT, Silver J (2017) Phasic inhibition as a mechanism for generation of rapid respiratory rhythms. Proc Natl Acad Sci U S A 114:12815–12820.

Daniel Gómez C, Rasmussen CM, Rekling JC (2021) GABAergic inhibition of presynaptic Ca(2+) transients in respiratory preBötzinger neurons in organotypic slice cultures. eNeuro 8:ENEURO.0154-21.2021.

Del Negro CA, Kam K, Hayes JA, Feldman JL (2009) Asymmetric control of inspiratory and expiratory phases by excitability in the respiratory network of neonatal mice in vitro. J Physiol 587:1217–1231.

Del Negro CA, Funk GD, Feldman JL (2018) Breathing matters. Nat Rev Neurosci 19:351–367.

Dong C, Zheng Y, Long-Iyer K, Wright EC, Li Y, Tian L (2022) Fluorescence imaging of neural activity, neurochemical dynamics, and drug-specific receptor conformation with genetically encoded sensors. Annu Rev Neurosci 45:273–294.

Gray PA, Rekling JC, Bocchiaro CM, Feldman JL (1999) Modulation of respiratory frequency by peptidergic input to rhythmogenic neurons in the preBötzinger complex. Science 286:1566–1568.

Guerrier C, Hayes JA, Fortin G, Holcman D (2015) Robust network oscillations during mammalian respiratory rhythm generation driven by synaptic dynamics. Proc Natl Acad Sci U S A 112:9728–9733.

Haji A, Okazaki M, Ohi Y, Yamazaki H, Takeda R (2003) Biphasic effects of morphine on bulbar respiratory neuronal activities in decerebrate cats. Neuropharmacology 45:368–379.

Hayes JA, Kottick A, Picardo MCD, Halleran AD, Smith RD, Smith GD, Saha MS, Del Negro CA (2017) Transcriptome of neonatal preBötzinger complex neurones in Dbx1 reporter mice. Sci Rep 7:8669.

Ikeda K, Kawakami K, Onimaru H, Okada Y, Yokota S, Koshiya N, Oku Y, Iizuka M, Koizumi H (2017) The respiratory control mechanisms in the brainstem and spinal cord: integrative views of the neuroanatomy and neurophysiology. J Physiol Sci 67:45–62.

Inyushkin AN (2007) Effects of leucine-enkephalin on potassium currents in neurons in the rat respiratory center in vitro. Neurosci Behav Physiol 37:739–746.

Johnson SM, Smith JC, Feldman JL (1996) Modulation of respiratory rhythm in vitro: role of Gi/o protein-mediated mechanisms. J Appl Physiol (1985) 80:2120–2133.

Kallurkar PS, Picardo MCD, Sugimura YK, Saha MS, Conradi Smith GD, Del Negro CA (2022) Transcriptomes of electrophysiologically recorded Dbx1-derived respiratory neurons of the preBötzinger complex in neonatal mice. Sci Rep 12:2923.

Koizumi H, Koshiya N, Chia JX, Cao F, Nugent J, Zhang R, Smith JC (2013) Structural-functional properties of identified excitatory and inhibitory interneurons within pre-Bötzinger complex respiratory microcircuits. J Neurosci 33:2994–3009.

Koizumi H, Mosher B, Tariq MF, Zhang R, Koshiya N, Smith JC (2016) Voltage-dependent rhythmogenic property of respiratory pre-Bötzinger complex glutamatergic, Dbx1-derived, and somatostatin-expressing neuron populations revealed by graded optogenetic inhibition. eNeuro 3: ENEURO.0081-16.2016.

Kottick A, Del Negro CA (2015) Synaptic depression influences inspiratory-expiratory phase transition in Dbx1 interneurons of the preBötzinger complex in neonatal mice. J Neurosci 35:11606–11611.

Krey RA, Goodreau AM, Arnold TB, Del Negro CA (2010) Outward currents contributing to inspiratory burst termination in preBötzinger complex neurons of neonatal mice studied in vitro. Front Neural Circuits 4:124.

Levitt ES, Abdala AP, Paton JF, Bissonnette JM, Williams JT (2015) μ Opioid receptor activation hyperpolarizes respiratory-controlling Kölliker-Fuse neurons and suppresses post-inspiratory drive. J Physiol 593:4453–4469.

Liu S, Kim DI, Oh TG, Pao GM, Kim JH, Palmiter RD, Banghart MR, Lee KF, Evans RM, Han S (2021) Neural basis of opioid-induced respiratory depression and its rescue. Proc Natl Acad Sci U S A 118e2022134118.

Maeda T, Shimoshige Y, Mizukami K, Shimohama S, Kaneko S, Akaike A, Satoh M (1995) Patch sensor detection of glutamate release evoked by a single electrical shock. Neuron 15:253–257.

Marvin JS, et al. (2018) Stability, affinity, and chromatic variants of the glutamate sensor iGluSnFR. Nat Methods 15:936–939.

Miller JR, Zuperku EJ, Stuth EAE, Banerjee A, Hopp FA, Stucke AG (2017) A subregion of the parabrachial nucleus partially mediates respiratory rate depression from intravenous remifentanil in young and adult rabbits. Anesthesiology 127:502–514.

Montandon G, Qin W, Liu H, Ren J, Greer JJ, Horner RL (2011) PreBötzinger complex neurokinin-1 receptor-expressing neurons mediate opioid-induced respiratory depression. J Neurosci 31:1292–1301.

Montandon G, Ren J, Victoria NC, Liu H, Wickman K, Greer JJ, Horner RL (2016) G-protein-gated inwardly rectifying potassium channels modulate respiratory depression by opioids. Anesthesiology 124:641–650.

Pace RW, Mackay DD, Feldman JL, Del Negro CA (2007) Inspiratory bursts in the preBötzinger complex depend on a calcium-activated non-specific cation current linked to glutamate receptors in neonatal mice. J Physiol 582:113–125.

Palkovic B, Marchenko V, Zuperku EJ, Stuth EAE, Stucke AG (2020) Multi-level regulation of opioid-induced respiratory depression. Physiology (Bethesda) 35:391–404.

Palkovic B, Cook-Snyder D, Callison JJ, Langer TM 3rd, Nugent R, Stuth EAE, Zuperku EJ, Stucke AG (2022) Contribution of the caudal medullary raphe to opioid induced respiratory depression. Respir Physiol Neurobiol 299:103855.

Phillips WS, Herly M, Del Negro CA, Rekling JC (2016) Organotypic slice cultures containing the preBötzinger complex generate respiratory-like rhythms. J Neurophysiol 115:1063–1070.

Phillips WS, Del Negro CA, Rekling JC (2018) Dendritic A-current in rhythmically active preBötzinger complex neurons in organotypic cultures from newborn mice. J Neurosci 38:3039–3049.

Picardo MC, Weragalaarachchi KT, Akins VT, Del Negro CA (2013) Physiological and morphological properties of Dbx1-derived respiratory neurons in the pre-Bötzinger complex of neonatal mice. J Physiol 591:2687–2703.

Ramirez JM, Baertsch N (2018) Defining the rhythmogenic elements of mammalian breathing. Physiology (Bethesda) 33:302–316.

Ramirez JM, Burgraff NJ, Wei AD, Baertsch NA, Varga AG, Baghdoyan HA, Lydic R, Morris KF, Bolser DC, Levitt ES (2021) Neuronal mechanisms underlying opioid-induced respiratory depression: our current understanding. J Neurophysiol 125:1899–1919.

Rekling JC, Champagnat J, Denavit-Saubié M (1996) Electroresponsive properties and membrane potential trajectories of three types of inspiratory neurons in the newborn mouse brain stem in vitro. J Neurophysiol 75:795–810.

Rekling JC, Shao XM, Feldman JL (2000) Electrical coupling and excitatory synaptic transmission between rhythmogenic respiratory neurons in the preBötzinger complex. J Neurosci 20:RC113.

Revill AL, Katzell A, Del Negro CA, Milsom WK, Funk GD (2021) KCNQ current contributes to inspiratory burst termination in the pre-Bötzinger complex of neonatal rats in vitro. Front Physiol 12:626470.

Richter DW, Smith JC (2014) Respiratory rhythm generation in vivo. Physiology (Bethesda) 29:58–71.

Song H, Hayes JA, Vann NC, LaMar MD, Del Negro CA (2015) Mechanisms leading to rhythm cessation in the respiratory preBötzinger complex due to piecewise cumulative neuronal deletions. eNeuro 2:ENEURO.0031-15.2015.

Sun X, Thörn Pérez C, Halemani DN, Shao XM, Greenwood M, Heath S, Feldman JL, Kam K (2019) Opioids modulate an emergent rhythmogenic process to depress breathing. Elife 8:e50613.

Takeda S, Eriksson LI, Yamamoto Y, Joensen H, Onimaru H, Lindahl SG (2001) Opioid action on respiratory neuron activity of the isolated respiratory network in newborn rats. Anesthesiology 95:740–749.

Varga AG, Reid BT, Kieffer BL, Levitt ES (2020) Differential impact of two critical respiratory centres in opioid-induced respiratory depression in awake mice. J Physiol 598:189–205.

Wei AD, Ramirez JM (2019) Presynaptic mechanisms and KCNQ potassium channels modulate opioid depression of respiratory drive. Front Physiol 10:1407.

Zavala-Tecuapetla C, Aguileta MA, Lopez-Guerrero JJ, González-Marín MC, Peña F (2008) Calcium-activated potassium currents differentially modulate respiratory rhythm generation. Eur J Neurosci 27:2871–2884.

Zhang J, Chen L, He Y, Ding Y, Zhou H, Hu H, Tang Y, Zheng Y (2010) Large-conductance calcium-activated potassium channels in the neurons of pre-Bötzinger complex and their participation in the regulation of central respiratory activity in neonatal rats. Neurosci Lett 481:159–163.